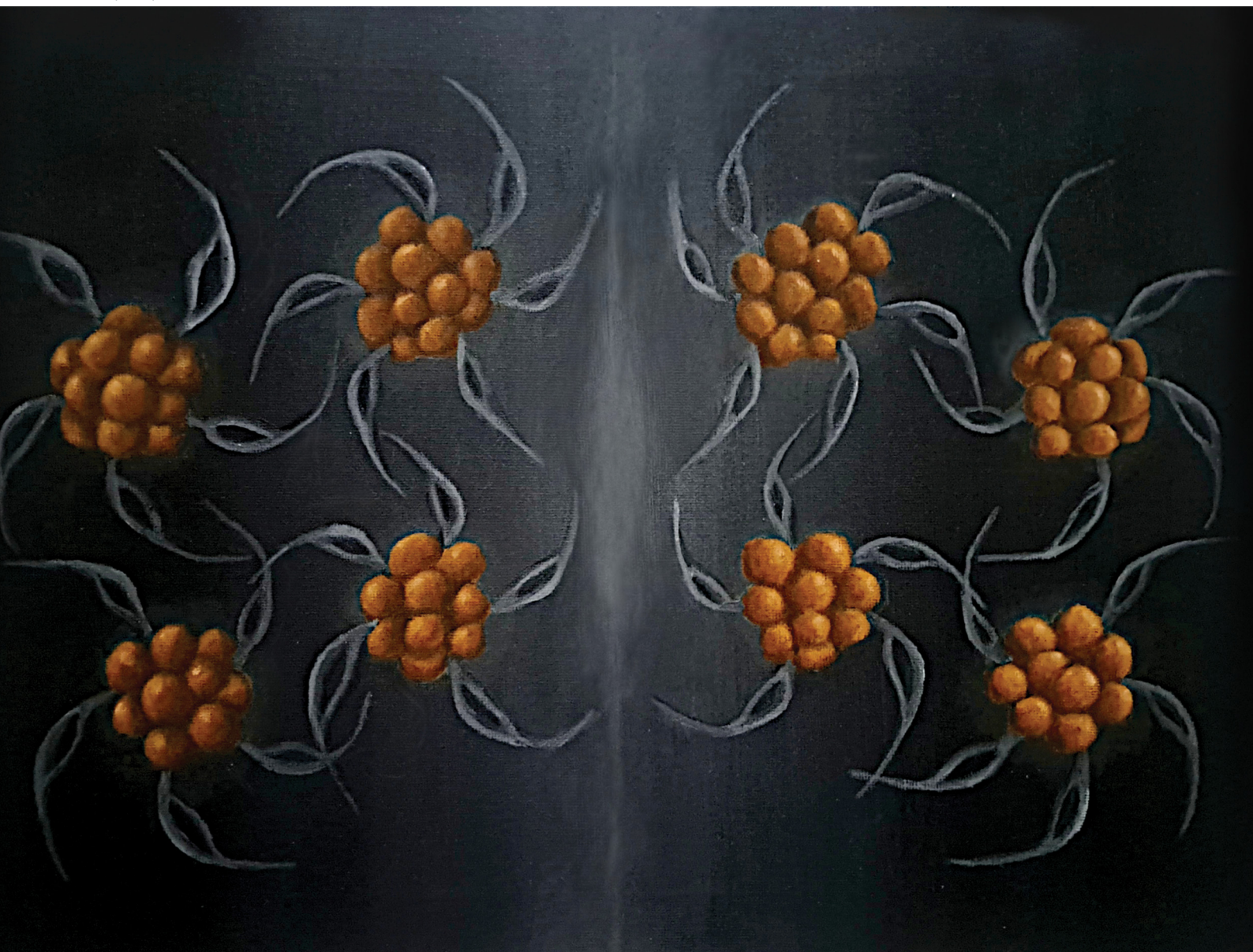


PCCP

Physical Chemistry Chemical Physics

rsc.li/pccp



ISSN 1463-9076

PAPER

Hanna Jääskö *et al.*
Optical properties of metal-ion-mediated Au₂₅
nanocluster-based assemblies



Cite this: *Phys. Chem. Chem. Phys.*, 2026, **28**, 12196

Optical properties of metal-ion-mediated Au₂₅ nanocluster-based assemblies

Hanna Jääskö,^a Sami Malola^a and Hannu Häkkinen^{ib}*^{ab}

Building cluster assemblies from superatomic building blocks, where each cluster behaves analogously to an elemental atom, has attracted interest in the past few decades due to their enhanced optical properties. Herein, we study the optical properties of recently discovered gold nanocluster assemblies mediated by Mg²⁺, Co²⁺, Ni²⁺ and Cu²⁺ metal ions [S. Kim *et al.*, *J. Am. Chem. Soc.*, 2025, **147**(34), 30803–30808] using time-dependent density functional theory. Depending on the coordinating metal ion, the assemblies exhibited different absorption spectra with a redshift of up to 51 nm. Surprisingly, our calculations revealed that the assemblies exhibit chiroptical response, despite being assembled from achiral building blocks. The chirality emerges from the coordination complex formed between the coordinating metal ions and the clusters' ligands and is transferred to the achiral nanoclusters. These theoretical findings may motivate researchers to create enantiopure nanocluster assemblies where spin conductivity is controlled by chirality.

Received 23rd January 2026,
Accepted 13th April 2026

DOI: 10.1039/d6cp00252h

rsc.li/pccp

1. Introduction

Cluster-assembled materials (CAMs) constructed from atomically precise noble metal nanoclusters (NCs) are emerging as promising platforms for application in nanoelectronics,^{1–6} bioimaging and -sensing,⁷ gas storage and -sensing^{8,9} and cancer theranostics¹⁰ and diagnosis.¹¹ Their electronic and optical properties can be finely tuned by modifying parameters such as intercluster distance, type of ligand or metal core.^{12–14} These nanoclusters can exhibit superatomic behavior, and they resemble the electronic structure and chemistry of individual atoms in the periodic table,¹⁵ following an early concept of building crystals from superatom building blocks.^{16,17} This concept has evolved significantly over the past few decades due to a better understanding of the self-assembly of clusters.^{18,19}

Self-assembly of metal NCs can be directed by various methods, including hydrogen-bonding, electrostatic interactions, C–H···π/π···π interactions, van der Waals interactions and coordination-assisted assembly.²⁰ Introducing a coordinating metal ion into the cluster network enables tuning of intercluster interactions, which have been reported to influence both conductivity²¹ and photophysical properties.^{22–24} Zn²⁺ assisted assembly of gold nanoclusters (AuNCs) has been extensively studied, and the complexation reaction with Zn has been found to significantly enhance photoluminescence, electrochemiluminescence and quantum yield (QY) of the

NCs.^{23,25–30} Other metal ions, such as Ca²⁺ and Sn²⁺, have also been employed in the self-assembly of AuNCs, leading to similar improvements in optical properties and, in some cases, enhanced photocatalytic activity.^{31,32}

These interesting and improved properties arise from the coordinating metal ion's influence on the ligand layer and, consequently, on the gold core. In coordination-assisted assemblies, the coordinating ion can enhance photoluminescence by restricting the motion of the surface ligands (inter- or intracuster motion), thereby suppressing nonradiative relaxation pathways.^{33–35} Therefore, coordination assemblies can offer new properties not present in individual NCs.³⁶ For example, metal-ion-coordinated assemblies can exhibit circularly polarized luminescence (CPL) despite being composed of achiral components.³⁷ Moreover, it is possible to control the assembly and disassembly of metal-ion-coordinated AuNCs, offering a promising strategy for developing drug-delivery materials.²⁹ Coordination-assisted assembly provides an interesting way to create and study chiral materials, since AuNC chirality is typically either an intrinsic property or induced by chiral ligands.³⁸

Recently, Kim *et al.* reported the synthesis of four novel single crystals formed from [Au₂₅(*p*-MBA)₁₈][–] (where *p*-MBA = *p*-mercaptobenzoic acid) in combination with Mg²⁺, Co²⁺, Ni²⁺, or Cu²⁺ ions, namely, Au₂₅–Mg, Au₂₅–Co, Au₂₅–Ni and Au₂₅–Cu.²⁴ The study revealed that shorter intercluster distances can enhance charge transport by up to 31-fold. While density functional theory (DFT) calculations reproduced the trends in the measured band gaps, giving also insight into possible conduction mechanisms, the optical properties of these CAMs were not studied computationally in ref. 24. Therefore, in this

^a Department of Physics, Nanoscience Center, University of Jyväskylä, Jyväskylä 40014, Finland. E-mail: hannu.j.hakkinen@ju.fi

^b Department of Chemistry, Nanoscience Center, University of Jyväskylä, Jyväskylä 40014, Finland



work, we investigate the optical properties of Au₂₅-based CAMs reported in ref. 24, focusing on how intercluster interactions and the structural organization influence their absorption and circular dichroism (CD) spectra. To this end, we performed ground-state DFT and linear-response time-dependent DFT (LR-TDDFT) calculations to study the optical properties. Interestingly, the assembly of achiral building blocks results in chiral structures, with CD intensities depending strongly on the coordinating metal ion. Our calculations reveal that the chirality originates from the coordination complex and is transferred to the individual clusters. Moreover, the absorption spectra vary significantly with the coordinating metal ion, resulting in a maximum shift of 51 nm between the assemblies.

2. Computational details

The assemblies shown in Fig. 1a–d, namely, Au₂₅-Mg, Au₂₅-Co, Au₂₅-Ni and Au₂₅-Cu, are simplified models based on the crystal structures reported by Kim *et al.*²⁴ (Fig. S1). A connecting node (Fig. 1e and f) together with its four attached clusters was extracted from the original crystal structures to reduce the computational cost, since performing LR-TDDFT on the full periodic crystal unit cell is not feasible. To see the extent of the collective effects on the cluster assemblies, one [Au₂₅(*p*-MBA)₁₈][−] cluster was isolated from each system, and the same calculations with the same level of theory were repeated, with more details provided in

Section S1 of the SI. Cobalt, nickel, and copper have partially filled 3d orbitals, which result in unpaired spins and thus require spin to be explicitly considered in calculations.

We employed the grid-based projector-augmented wave (GPAW)³⁹ code for all the DFT calculations. We used the Gritsenko–van Leeuwen–van Lenthe–Baerends solid-correlation (GLLB-SC)⁴⁰ functional for single-point ground state calculations with structures taken directly from the reported crystal structures²⁴ and the Perdew–Burke–Ernzerhof (PBE) functional⁴¹ as the exchange–correlation kernel for the LR-TDDFT calculations. Oscillator and rotatory strengths obtained from the LR-TDDFT calculations were broadened using 0.1 eV Gaussians. All calculations were performed in a non-periodic unit cell with a 6.0 Å buffer between the cell surface and the surface of the cluster assembly. All numerical calculations were performed in a real-space grid with a spacing of 0.25 Å. The total charge of the cluster assemblies was set to $-4|e|$, originating from the four [Au₂₅(*p*-MBA)₁₈][−] clusters, which have a closed shell 8 electron superatom configuration.²⁴ For the assembly with Mg metal ions, the calculations were performed as spin-paired, and for Co, Ni and Cu containing assemblies, spin-polarized. An energy cut-off of 2.5 eV was used for the assemblies and individual clusters in LR-TDDFT calculations. This ensures convergence of the spectra at and close to the optical gap (Fig. S2). To study the origins of the absorption peaks obtained from the LR-TDDFT calculations, we performed the transition contribution map (TCM) analysis.⁴² More details on the computational methods can be found in Section S2 of the SI.

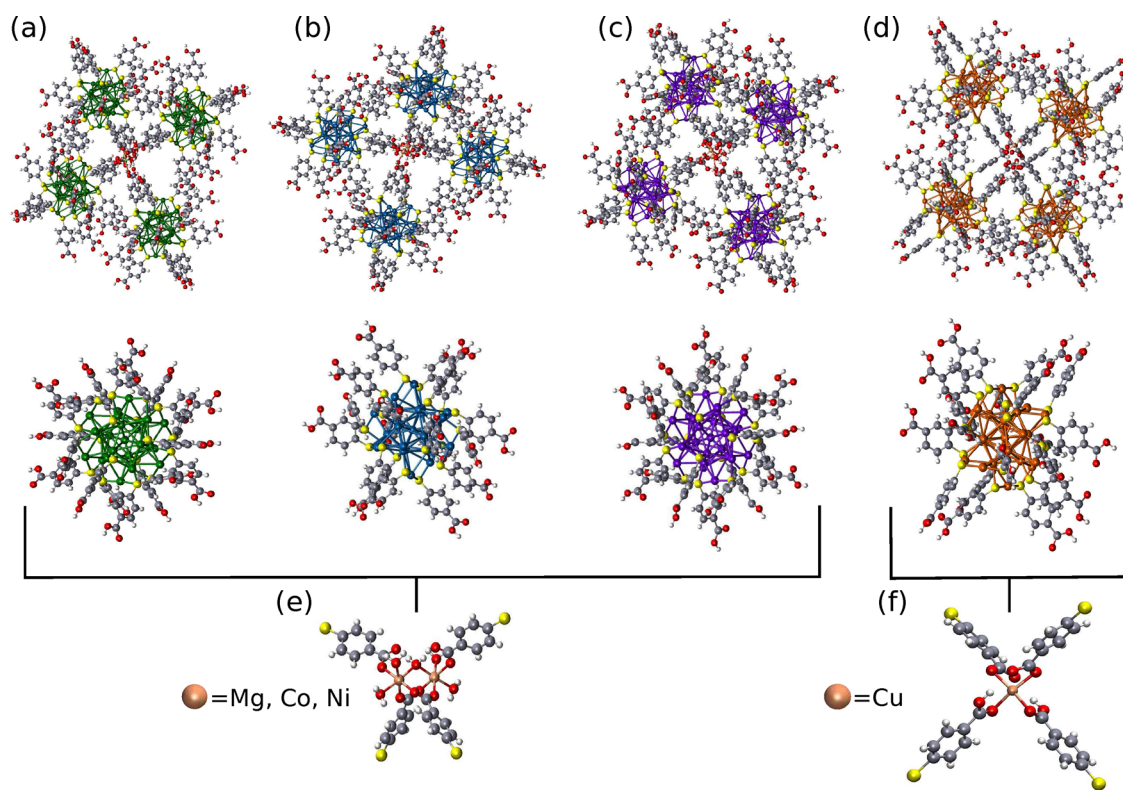


Fig. 1 Structures of (a) Mg, (b) Co, (c) Ni, and (d) Cu mediated [Au₂₅(*p*-MBA)₁₈][−] assemblies, together with their isolated [Au₂₅(*p*-MBA)₁₈][−] cluster, represented in green, blue, violet, and orange, respectively. (e) The connecting node for (a)–(c), and (f) the connecting node for (d). C, O, H and S atoms are shown in gray, red, white, and yellow, respectively.



3. Results and discussion

3.1. Structural changes

We start by discussing the small variations in the clusters' structure in the four cluster assemblies, induced by packing and small variations from the coordinating ion. We concentrate here on the details of the S–Au–S surface motifs around the metal cluster cores. Fig. 2a shows that Au₂₅–Mg has a standard

deviation of 0.23° for the S–Au–S motifs, while Au₂₅–Cu has 4.57°. The differences between these two endpoints are shown in Fig. 2b for [Au₂₅(*p*-MBA)₁₈][−] clusters taken from Au₂₅–Mg and Au₂₅–Cu assemblies. This indicates that the Cu²⁺ ion has influenced the ligand layer the most, thereby possibly altering its optical response and electronic band structure more than in the other systems. The differences in the Cu assembly's properties are likely to arise from the different coordination complexes compared to other systems. However, the Mg, Co and Ni assemblies are otherwise identical, except for the metal ion. Mg belongs to the s-block elements, while Co and Ni belong to the d-block and have open-shell electronic structures. Therefore, the transition metal coordinating ions might be more reactive than Mg atoms with a full valence shell, causing the observed changes.

3.2. Absorption spectra

Fig. 3a–d shows the absorption spectra of each assembly together with their corresponding individual [Au₂₅(*p*-MBA)₁₈][−] cluster's spectra. As the intercluster distance decreases, the optical band-gap decreases (Table 1), indicating stronger electronic coupling between the NCs. This result is consistent with the experimental results on the optical gaps reported by Kim *et al.*,²⁴ also shown in Table 1. We also note that the intensity of the lowest-energy absorption peak of each assembly is roughly four times larger than that of the individual cluster. This indicates a rather linear increase in the transition dipole moment for this transition in the assembly.

Fig. S3 presents the absorption spectra of the assemblies in the energy axis, along with the individual oscillator strengths for the electronic transitions. Au₂₅–Mg shows a few strong and well-defined electronic transitions, whereas the other systems have many transitions close to the same wavelength. Consequently, their spectra are broader and less intense compared to that of Au₂₅–Mg. In the case of Au₂₅–Cu, a second peak appears around 650 nm. Surprisingly, the individual [Au₂₅(*p*-MBA)₁₈][−] cluster taken from the assembly also has a second absorption peak, which is not prominent in any of the other systems or in their individual clusters. A possible explanation for these observations comes from the different coordination environments of the assemblies. In Au₂₅–Mg, Au₂₅–Co, and Au₂₅–Ni, two coordinating metal ions and five water molecules connect the clusters, while in Au₂₅–Cu, only one such ion is present without water molecules. Consequently, the former assemblies are slightly more structurally constrained, whereas the latter may allow greater freedom of motion and flexibility in ligand arrangement. Although DFT calculations cannot capture the dynamics of the ligands, it is possible that restricted ligand motion also influences the photophysical properties of these assemblies, as has previously been observed for many CAMs.^{23,28,32,34,35}

To understand the absorption peaks, we performed transition contribution (TCM) analysis along with the projected density of states (PDOS) resolved by atom type. This analysis allows us to identify which atoms or parts of the structures are responsible for the observed electronic transitions. For the Au₂₅–Co, Au₂₅–Ni, and Au₂₅–Cu assemblies, the TCMs are

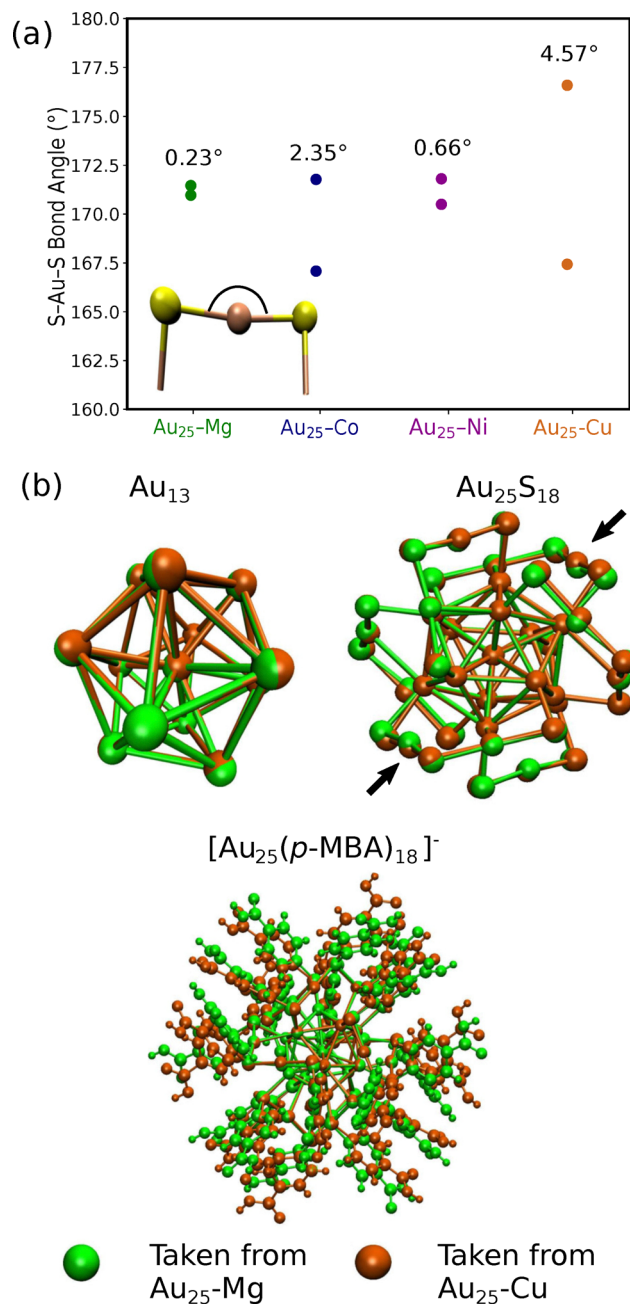


Fig. 2 (a) Distribution of the S–Au–S bond angles along with their standard deviation. (b) Aligned Au₂₅ clusters taken from Au₂₅–Mg and Au₂₅–Cu assemblies, highlighting differences in the S–Au–S motifs' bond angles and the resulting variations in ligand positions. On the left is the icosahedral core, on the right is the gold core with the Au–S interface and at the bottom is the whole cluster with the ligand layer as well.



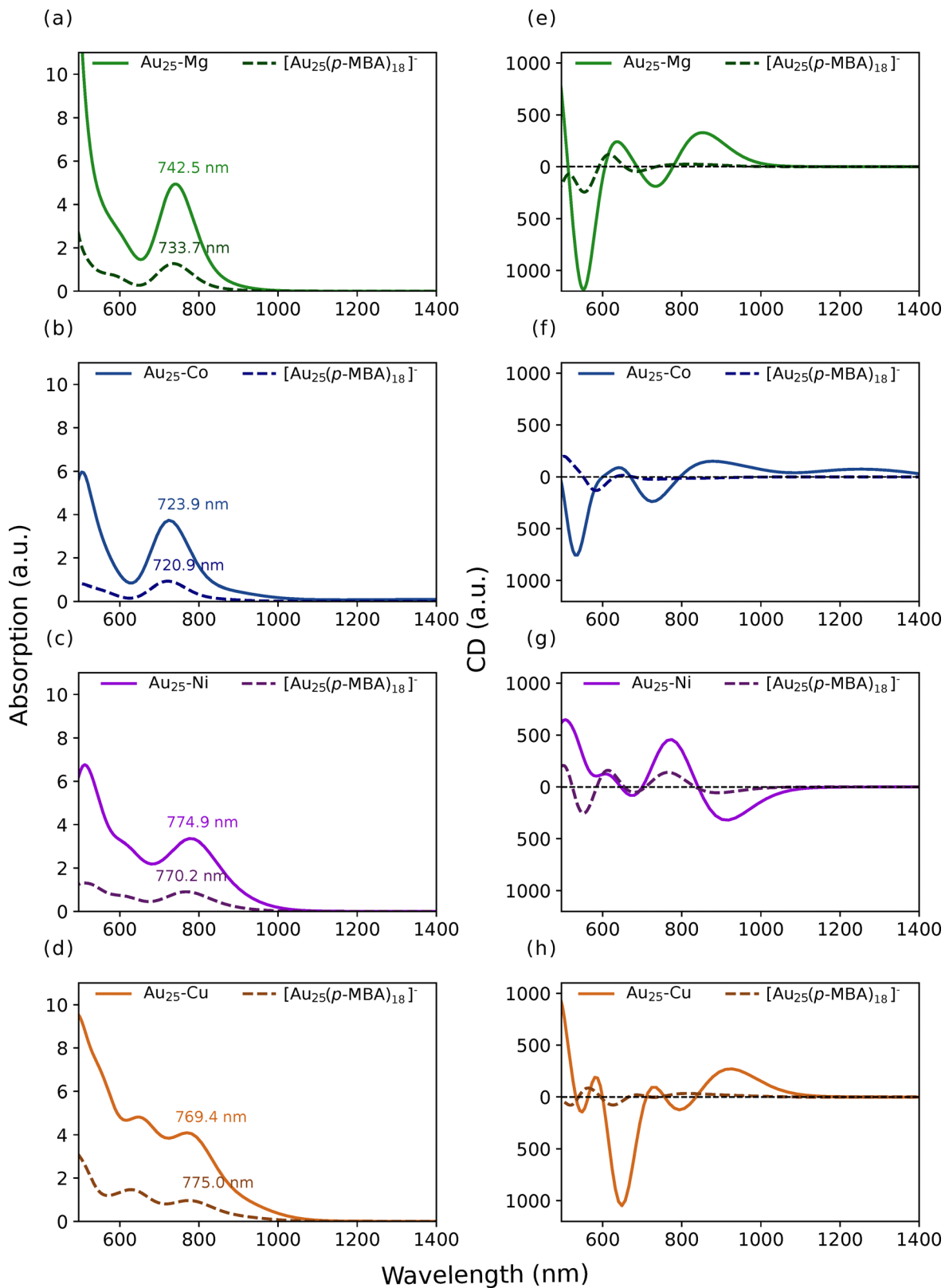


Fig. 3 Calculated (a)–(d) absorption spectra and (e)–(h) CD spectra of all four Au₂₅ cluster assemblies (solid lines) and their corresponding isolated [Au₂₅(p-MBA)₁₈]⁻ nanoclusters (dashed lines), shown in order of decreasing intercluster distance.



Table 1 Intercluster distances, measured optical gaps,²⁴ calculated optical gaps and HOMO–LUMO gaps for the cluster assemblies. For spin-polarized calculations, both spin up and spin down HOMO–LUMO gaps are shown

System	Intercluster distance (Å)	Exp. optical gap ²⁴ (eV)	Calc. optical gap (eV)	HOMO–LUMO gap (eV)
Au ₂₅ –Mg	22.151	1.37	1.43	1.24
Au ₂₅ –Co	22.142	1.32	1.40	(Up) 1.27 (Down) 1.25
Au ₂₅ –Ni	22.058	1.30	1.31	(Up) 1.13 (Down) 1.10
Au ₂₅ –Cu	21.524	1.23	1.29	(Up) 0.96 (Down) 0.43

shown separately for spin up and spin down channels. The first absorption peak of Au₂₅–Mg and Au₂₅–Co originates mainly from Au to Au transitions (HOMO to LUMO), shown in Fig. S4 and Fig. S5, respectively. In the case of Au₂₅–Ni, the spin down channel exhibits a strong Au to Au transition, while the spin up channel exhibits an Au to Au as well as Au to Au–S and Au to ligand transitions (Fig. S6). The TCM analysis of the first absorption peak of Au₂₅–Cu (Fig. S7a and b) also indicates Au to Au transitions for both spin channels, with the spin down channel exhibiting a slightly higher energy transition. The second absorption peak shows Au to ligand transitions for both spins, shown in Fig. S7c and d.

In all these assemblies, the first absorption peak is mainly caused by the Au to Au transitions (HOMO to LUMO), verified by the TCM analysis. The superatomic nature of these assemblies has been discussed before,²⁴ where it was confirmed that the nanoclusters retain their eight-electron closed-shell superatomic behavior. They consist of three occupied P-symmetric states and empty D-symmetric states near the Fermi level. Therefore, the first peak is caused by the superatomic P to D transitions, which then determines the optical and HOMO–LUMO gaps.

Fig. S8–S10 display the frontier molecular orbitals of Au₂₅–Mg, Co and Ni assemblies, along with their projected density of states into atom types. From there, it can be observed that the four highest occupied molecular orbitals are mostly located in the clusters and slightly on the ligands. The lowest unoccupied molecular orbitals are also located mainly in the clusters and ligands. The orbitals are slightly more spread toward the ligand ends in Co and Ni assemblies. Au₂₅–Ni exhibits a noticeable DOS contribution from the coordinating metal ion, although not near the Fermi level. Au₂₅–Mg and Au₂₅–Co do not show any significant contributions from the metal ion. Furthermore, Au₂₅–Cu differs from the other systems, since its HOMO–LUMO transition for the spin down channel is from the cluster to the coordinating metal center, as shown in Fig. S11. However, the TCM analysis shows that the first absorption peak is not due to this transition but rather due to the Au to Au transition.

An interesting question is whether these assemblies have a plasmonic nature or not. It is well known that Au₂₅ exhibits molecule-like optical transitions. However, when many of these clusters are brought together, collective electronic excitations could, in principle, emerge. Nevertheless, we observe quite sharp absorption peaks (Fig. 3), which, according to the TCM analysis, arise from the HOMO to LUMO transitions localized

on the clusters. The results suggest the presence of four independent excitations associated with the individual clusters rather than a single collective excitation (see Fig. S12). The induced transition density in Fig. S12 also shows formation of parallel transition dipoles in the assembly which may straightforwardly explain the approximate linear increase in the absorption intensity in the assembly as compared to isolated clusters (Fig. 3).

3.3. CD spectra and chirality of the coordination complex

CD spectra are presented in Fig. 3e–h. All four assemblies exhibit CD activity, but the peak positions and intensities vary. Interestingly, the first CD peak of Au₂₅–Cu appears at a longer wavelength compared to Au₂₅–Mg, suggesting more prominent changes in the Au–S interface, likely associated with the decreased intercluster distance. In all cases, the most intense peaks appear at shorter wavelengths, originating primarily from the ligand layer, confirmed by the rotational transition contribution map analysis for Au₂₅–Mg (Fig. S13). The low intensity peak of Au₂₅–Co at longer wavelengths is explained in Section S2 of the SI.

In the crystal structures, both left- and right-handed coordination complexes exist, which determine the handedness of the cluster assembly. In the case of Au₂₅–Ni, an opposite handed assembly was chosen for the ground state and linear response calculations, resulting in an opposite CD signal to the other assemblies. Moreover, Au₂₅–Mg assemblies were identified and evaluated for both handedness and the CD spectra (Fig. S14) confirmed their perfectly mirrored CD signals.

In order to understand the unexpected chirality in the assemblies, we extracted the coordination center from each assembly, shown in Fig. 1e and f, and recorded CD spectra for both left- and right-handed enantiomers (Fig. 4), and compared those to the assemblies' CD spectra. The spectra of the individual coordination centers differ, which helps to explain the origin of chirality in the corresponding cluster assemblies. For example, the first CD peak of the magnesium coordination complex appears around 260 nm (Fig. 4a), while the Au₂₅–Mg assembly exhibits a first peak at a longer wavelength, around 855 nm. This clearly indicates that the chirality is transferred from the coordination center to the clusters. For Ni, Co and Cu coordination complexes (Fig. 4b–d), the first peaks occur at longer wavelengths, although the more intense peaks remain in the same region as for the Mg coordination complex. Among the four, the Cu coordination complex has the strongest CD



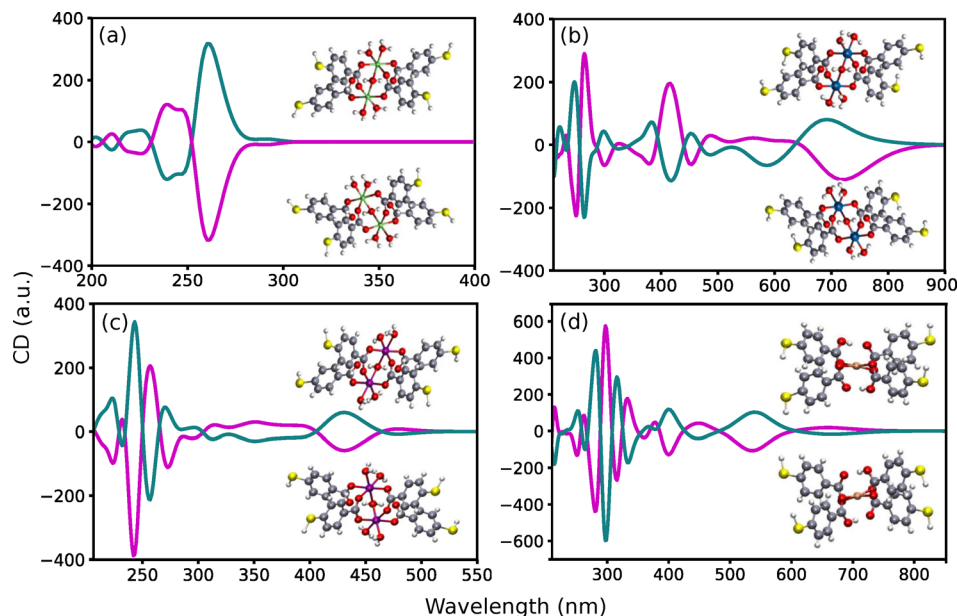


Fig. 4 CD spectra of both enantiomers of (a) Mg, (b) Co, (c) Ni, and (d) Cu complexes. The insets show the corresponding enantiomers.

signal around 300 nm. Consequently, the Au₂₅-Cu assembly has the first CD peak at longer wavelengths compared to the other assemblies, suggesting that the chirality transfer is most pronounced in this system. A possible explanation for this is the different coordination environment between the systems. In the case of Au₂₅-Mg, Co and Ni assemblies, the 2 metal ions bridged together with a water molecule could be considered as the chiral center. Interestingly, Cu assembly has only one metal ion, and the four ligands are connected to it in a chiral manner, distinguishing it from the other assemblies.

Based on the CD spectra of the coordination complexes, we did not repeat calculations for the other enantiomers of the full cluster assemblies Au₂₅-Co, Au₂₅-Ni and Au₂₅-Cu since we expect them to behave similarly. Upon further investigation, we found that the crystal structures have repeated “layers” of both enantiomers, visualized in Fig. S15 for Au₂₅-Mg and Au₂₅-Cu.

4. Conclusions

Time-dependent density functional theory calculations were performed for four Au₂₅ cluster-assembled materials, Au₂₅-Mg, Au₂₅-Co, Au₂₅-Ni and Au₂₅-Cu, to study their optical properties. The structures exhibited different absorption intensities at different wavelengths, depending on the coordinating metal ion in the coordination bonds between carboxylic acids. Remarkably, the assemblies exhibited circular dichroism (CD) signals at various wavelengths and with varying intensities. For each coordination complex, both left- and right-handed enantiomers were present in the crystal structures. The enantiomers formed layers of right- and left-handed structures. This information may motivate efforts to experimentally guide the assembly process towards enantiopure assemblies with a chosen

handedness. Coupled with the fact that assemblies with Co²⁺, Ni²⁺, and Cu²⁺ ions have two spin channels, these 2D or meta-2D materials might have intriguing conductance properties due to chirality-induced spin selectivity (CISS) effects.^{43,44}

Author contributions

H. J.: conceptualization, investigation, formal analysis, and writing the original draft. S. M.: conceptualization, editing and reviewing the manuscript draft. H. H.: conceptualization, supervision, editing and reviewing the manuscript draft, and funding acquisition.

Conflicts of interest

There are no conflicts to declare.

Data availability

The data supporting this article have been included as part of the supplementary information (SI). See DOI: <https://doi.org/10.1039/d6cp00252h>.

Acknowledgements

This work is associated with the Finnish Quantum Institute and was supported by the Finnish Ministry of Education and Culture through the Quantum Doctoral Education Pilot Program (QDOC) and by the Research Council of Finland through the Finnish Quantum Flagship Project (359240). The simulations and DFT analysis were performed at the Finnish National Supercomputing Center (CSC) using the Mahti supercomputer. We thank the group of Sarah Park for numerous inspiring



discussions on cluster-assembled materials and Timo Weckman and Maria Francisca Matus for helpful technical discussions and advice.

References

- 1 T. Higaki, J. C. Russell, D. W. Paley, X. Roy and R. Jin, *Chem. Sci.*, 2023, **14**, 13191–13197.
- 2 M. Reato, T. Dainese, S. Antonello and F. Maran, *Chem. Mater.*, 2021, **33**, 4177–4187.
- 3 M. Galchenko, A. Black, L. Heymann and C. Klinke, *Adv. Mater.*, 2019, **31**, 1900684.
- 4 Y. Zhu, L. Guo, J. Guo, L. Zhao, C. Li, X. Qiu, Y. Qin, X. Gu, X. Sun and Z. Tang, *Angew. Chem., Int. Ed.*, 2023, **62**, e202213208.
- 5 P. P. Dash, A. Kabiraj, G. Mallik, P. Kumari, S. N. Jha, Y. Kumar and S. Rath, *J. Appl. Phys.*, 2024, **136**, 164304.
- 6 A. K. Das, S. Biswas, A. Kayal, A. C. Reber, S. Bhandary, D. Chopra, J. Mitra, S. N. Khanna and S. Mandal, *Nano Lett.*, 2023, **23**, 8923–8931.
- 7 W. Zhang, D. Lin, H. Wang, J. Li, G. U. Nienhaus, Z. Su, G. Wei and L. Shang, *Bioconjugate Chem.*, 2017, **28**, 2224–2229.
- 8 S. Basu, S. Bhandari, U. N. Pan, A. Paul and A. Chattopadhyay, *J. Mater. Chem. C*, 2018, **6**, 8205–8211.
- 9 S. A. Claridge, A. W. Castleman, S. N. Khanna, C. B. Murray, A. Sen and P. S. Weiss, *ACS Nano*, 2009, **3**, 244–255.
- 10 S. Basu, U. Goswami, A. Paul and A. Chattopadhyay, *J. Mater. Chem. B*, 2018, **6**, 1650–1657.
- 11 W. Hou, F. Xia, G. Alfranca, H. Yan, X. Zhi, Y. Liu, C. Peng, C. Zhang, J. M. De La Fuente and D. Cui, *Biomaterials*, 2017, **120**, 103–114.
- 12 C. Sikorska, E. Vincent, A. Schnepf and N. Gaston, *Phys. Chem. Chem. Phys.*, 2024, **26**, 10673–10687.
- 13 Q. Li, J. C. Russell, T.-Y. Luo, X. Roy, N. L. Rosi, Y. Zhu and R. Jin, *Nat. Commun.*, 2018, **9**, 3871.
- 14 F. Fetzer, A. Maier, M. Hodas, O. Geladari, K. Braun, A. J. Meixner, F. Schreiber, A. Schnepf and M. Scheele, *Nat. Commun.*, 2020, **11**, 6188.
- 15 M. Walter, J. Akola, O. Lopez-Acevedo, P. D. Jadzinsky, G. Calero, C. J. Ackerson, R. L. Whetten, H. Grönbeck and H. Häkkinen, *Proc. Natl. Acad. Sci. U. S. A.*, 2008, **105**, 9157–9162.
- 16 S. N. Khanna and P. Jena, *Phys. Rev. Lett.*, 1992, **69**, 1664–1667.
- 17 S. N. Khanna and P. Jena, *Phys. Rev. B: Condens. Matter Mater. Phys.*, 1995, **51**, 13705–13716.
- 18 S. A. Claridge, A. Castleman, S. N. Khanna, C. B. Murray, A. Sen and P. S. Weiss, *ACS Nano*, 2009, **3**, 244–255.
- 19 P. Jena and Q. Sun, *Chem. Rev.*, 2018, **118**, 5755–5870.
- 20 J. V. Rival, P. Mymoon, K. M. Lakshmi, N. Nonappa, T. Pradeep and E. S. Shibu, *Small*, 2021, **17**, 2005718.
- 21 S. Ji, D. Peng, F. Sun, Q. You, R. Wang, N. Yan, Y. Zhou, W. Wang, Q. Tang, N. Xia, Z. Zeng and Z. Wu, *J. Am. Chem. Soc.*, 2023, **145**, 24012–24020.
- 22 S. Kim, H. Kim, C. Lee, I. Park, Y. Kim, D. Moon, J. H. Shim, S. Ryu and S. S. Park, *ACS Nano*, 2024, **18**, 29036–29044.
- 23 H.-Y. Huang, K.-B. Cai, M. J. Talite, W.-C. Chou, P.-W. Chen and C.-T. Yuan, *Sci. Rep.*, 2019, **9**, 4053.
- 24 S. Kim, H. Jääskö, K. C. Park, S. Malola, H. Häkkinen and S. S. Park, *J. Am. Chem. Soc.*, 2025, **147**, 30803–30808.
- 25 S. Basu, A. Paul and A. Chattopadhyay, *Chem. – Eur. J.*, 2017, **23**, 9137–9143.
- 26 S. Basu, A. Hajra, C. Gayen and A. Paul, *ChemPhysChem*, 2020, **21**, 809–813.
- 27 B. Kuppen and U. Maitra, *Nanoscale*, 2017, **9**, 15494–15504.
- 28 C. Gayen, S. Basu, U. Goswami and A. Paul, *Langmuir*, 2019, **35**, 9037–9043.
- 29 H. Chang, N. S. Karan, K. Shin, M. S. Bootharaju, S. Nah, S. I. Chae, W. Baek, S. Lee, J. Kim, Y. J. Son, T. Kang, G. Ko, S.-H. Kwon and T. Hyeon, *J. Am. Chem. Soc.*, 2021, **143**, 326–334.
- 30 Z.-C. Shen, Y.-T. Yang, Y.-Z. Guo, Y.-Q. Chai, J.-L. Liu and R. Yuan, *Anal. Chem.*, 2023, **95**, 5568–5574.
- 31 L. Wang, C. Zhang, T. Li, M. Duan, F. Xia, X. Li, C. Song, S. Pan, B. Liu and D. Cui, *Nanoscale*, 2019, **11**, 22237–22242.
- 32 S. Chandra, N. Nonappa, G. Beaune, A. Som, S. Zhou, J. Lahtinen, H. Jiang, J. V. I. Timonen, O. Ikkala and R. H. A. Ras, *Adv. Opt. Mater.*, 2019, **7**, 1900620.
- 33 Q. Yao, Z. Luo, X. Yuan, Y. Yu, C. Zhang, J. Xie and J. Y. Lee, *Sci. Rep.*, 2014, **4**, 3848.
- 34 D. Bain, A. Devi, R. Rashi, S. Chakraborty, S. Kolay and A. Patra, *J. Phys. Chem. C*, 2023, **127**, 18244–18251.
- 35 V. Tiwari, A. Bhattacharyya and T. Karmakar, *Nanoscale*, 2024, **16**, 15141–15147.
- 36 S. Basu, A. Paul and A. Chattopadhyay, *J. Mater. Chem. A*, 2016, **4**, 1218–1223.
- 37 S. Basu, M. P. Bakulić, Ž. S. Maršić, V. Bonačić-Koutecký and N. Amdursky, *ACS Nano*, 2023, **17**, 16644–16655.
- 38 S. Knoppe and T. Bürgi, *Acc. Chem. Res.*, 2014, **47**, 1318–1326.
- 39 J. J. Mortensen, A. H. Larsen, M. Kuisma, A. V. Ivanov, A. Taghizadeh, A. Peterson, A. Haldar, A. O. Dohn, C. Schäfer, E. Ö. Jónsson, E. D. Hermes, F. A. Nilsson, G. Kastlunger, G. Levi, H. Jónsson, H. Häkkinen, J. Fojt, J. Kangsabanik, J. Sødequist, J. Lehtomäki, J. Heske, J. Enkovaara, K. T. Winther, M. Dulak, M. M. Melander, M. Ovesen, M. Louhivuori, M. Walter, M. Gjerding, O. Lopez-Acevedo, P. Erhart, R. Warmbier, R. Würdemann, S. Kaappa, S. Latini, T. M. Boland, T. Bligaard, T. Skovhus, T. Susi, T. Maxson, T. Rossi, X. Chen, Y. L. A. Schmerwitz, J. Schiøtz, T. Olsen, K. W. Jacobsen and K. S. Thygesen, *J. Chem. Phys.*, 2024, **160**, 092503.
- 40 M. Kuisma, J. Ojanen, J. Enkovaara and T. T. Rantala, *Phys. Rev. B: Condens. Matter Mater. Phys.*, 2010, **82**, 115106.
- 41 J. P. Perdew, K. Burke and M. Ernzerhof, *Phys. Rev. Lett.*, 1996, **77**, 3865–3868.
- 42 S. Malola, L. Lehtovaara, J. Enkovaara and H. Häkkinen, *ACS Nano*, 2013, **7**, 10263–10270.
- 43 B. P. Bloom, Y. Paltiel, R. Naaman and D. H. Waldeck, *Chem. Rev.*, 2024, **124**, 1950–1991.
- 44 S.-H. Park and S. S. Park, *Trends Chem.*, 2026, **1**, 1.

